PCCP

ROYAL SOCIETY OF CHEMISTRY

PAPER

View Article Online
View Journal | View Issue

Cite this: *Phys. Chem. Chem. Phys.*, 2024, **26**, 14624

Molecular phosphorescence enhancement by the plasmon field of metal nanoparticles†

Niyazbek Kh. Ibrayev,*[a] Rashid R. Valiev, *[ab] Evgeniya V. Seliverstova,[a] Evgeniya P. Menshova,[a] Rinat T. Nasibullin[b] and Dage Sundholm [b]

Received 27th March 2024,
Accepted 26th April 2024

DOI: 10.1039/d4cp01281j

rsc.li/pccp

A theoretical model is proposed that allows the estimation of the quantum yield of phosphorescence of dye molecules in the vicinity of plasmonic nanoparticles. For this purpose, the rate constants of the radiative and nonradiative intramolecular transitions for rhodamine 123 (**Rh123**) and brominated rhodamine (**Rh123-2Br**) dyes have been calculated. The plasmon effect of Ag nanoparticles on various types of luminescence processes has been studied both theoretically and experimentally. We show that in the presence of a plasmonic nanoparticle, the efficiency of the immediate and delayed fluorescence increases significantly. The phosphorescence rate of the rhodamine dyes also increases near plasmonic nanoparticles. The long-lived luminescence *i.e.*, delayed fluorescence and phosphorescence is more enhanced for **Rh123-2Br** than for **Rh123**. The largest phosphorescence quantum yield is obtained when the dye molecule is at a distance of 4–6 nm from the nanoparticle surface. Our results can be used in the design of plasmon-enhancing nanostructures for light-emitting media, organic light-emitting diodes, photovoltaic devices, and catalysts for activation of molecular oxygen.

1. Introduction

Localized plasmon resonance (LPR) of metal nanoparticles (NPs) is used in many analytical methods and applications. The resonantly photoexcited collective oscillations of free electrons in metal NPs consisting of Ag, Au, Cu or Al lead to an enhancement of the electromagnetic field around the NP.[1] It is known that the enhancement factor of the strength of the electric field of plasmonic NPs can be as large as 10^4.[2] Fluorophore or analogous molecules located in the near such NPs are exposed to an intense external influence, which allows them to accelerate photocatalytic reactions and to induce metal-enhanced luminescence or Raman scattering (SERS).

Plasmon-enhanced fluorescence has been studied by several groups showing that the fluorescence of dye molecules can be enhanced or quenched by the NPs.[3–5] The plasmon effect is determined by the distance between the plasmonic NP and the emitting molecule and by the mutual orientation of their transition dipole moments. This phenomenon can be used in devices based on radiative processes and their decay. In particular, the LPR of metal NPs has a significant influence on the relaxation processes of photoexcited emitters due to the Purcell effect[6,7] making it possible to significantly reduce the lasing threshold of dye lasers in active media.[8,9] Plasmonic effects can also be used to create media with specified optical properties,[10,11] in sensor systems[12–14] and in optoelectronic devices.[15,16]

Particularly interesting is the question of the influence of plasmons on the long-term luminescence that is associated with spin effects. Long-lived triplet states are important in many fundamental processes and can also be used in various practical applications. For example, the long-term luminescence of molecular probes may be used in bioimaging. However, there is an urgent need to improve its signal-to-noise ratio, which is low due to the autofluorescence of biological tissues.[17] Triplet states are actively used in photosynthetic systems[18] for generating reactive species of molecular oxygen (ROS). Singlet oxygen is employed in photodynamic therapy for the deactivation of cancer cells,[19,20] in antibacterial therapy,[21,22] as well as for treating skin and respiratory diseases.[23] ROS are important in advanced oxidation processes for the degradation of pollutants in various resources,[24] as well as in photocatalytic and photovoltaic reactions.[25–28] Triplet states of organic compounds are also applicable in organic light-emitting diode (OLED) technologies,[29,30] in solar cells[31,32] and in transistors.[33,34]

Plasmon-enhanced phosphorescence is a very attractive area for many specialists.[35–40] The authors of ref. 35 studied the distance dependence of the eosin luminescence in anhydrous glycerol and obtained an approximately 9-fold increase in the fluorescence and an almost 4-fold increase in the delayed fluorescence and phosphorescence due to the plasmonic effect.

[a] *Institute of Molecular Nanophotonics, Buketov Karaganda University, 100024 Karaganda, Kazakhstan. E-mail: niazibrayev54@gmail.com*
[b] *Department of Chemistry, University of Helsinki, FI-00014 Helsinki, Finland. E-mail: rashid.valiev@helsinki.fi*

† Electronic supplementary information (ESI) available. See DOI: https://doi.org/10.1039/d4cp01281j

Metal-enhanced phosphorescence of rose bengal (RB) on silver island films (SIF) has been studied,[36] where a 5-fold increase in the phosphorescence intensity was registered. The authors of ref. 41 studied the plasmonic effect of gold NPs on homogeneous and heterogeneous triplet–triplet annihilation of methylene blue (MB) in the presence of Au NPs. The increased efficiency of the two processes is associated with an enhanced excitation rate of singlet molecules and an enhanced intersystem crossing (ISC) rate to the triplet state.[42] The plasmonic field of the NPs leads to a doubling of the population of the triplet state of MB through enhanced absorption by the singlet state of the molecule. In ref. 43, a 10-fold increase in the population of the triplet state of RB was achieved when molecules were placed near aggregates of gold NPs.

Silver nanoprisms can redistribute the probability of the decay of excited states of Pd–porphyrin,[44] which was achieved by controlling the LPR wavelength of the Ag nanoprism and by adjusting its distance to the luminophore molecule. A twofold increase in the efficiency of the phosphorescence emitted by a Pt–porphyrin film has been achieved by adding gold NPs that decrease the triplet–triplet quenching.[45] An increase in both fluorescence and phosphorescence and a decrease in their lifetime were observed for 2,5-dihexyloxy-4-bromobenzaldehyde in the presence of Ag NPs.[46] The increased phosphorescence is due to the increased photoabsorption and photoemission rates near the NP. We obtained similar results in our studies of the distance dependence of the plasmon-accelerated decay of excited singlet and triplet states of eosin molecules.[47] The plasmonic effect was manifested by the increased emission intensity, the shorter lifetime of the fluorescence, the delayed fluorescence, and by the phosphorescence. The optimal distance for the largest enhancement of all types of luminescence was 6–8 nm, which coincides rather well with the Förster radius of the non-radiative inductive-resonant process. A mathematical model was developed suggesting that the distance dependence of the intensity of the long-lived luminescence is qualitatively the same as the distance dependence of the fluorescence of a dye layer on a metal island film, which agree with experimental data. The influence of plasmonic NPs on the fluorescence and phosphorescence of erythrosine molecules in a polymer matrix has also been studied experimentally and theoretically.[48]

Even though many studies have been performed in this area, the mechanisms of the influence of plasmons on the deactivation of triplet states of organic molecules and on the phosphorescence is not elucidated. The radiative triplet ($T_1 \rightarrow S_0$) transition leading to phosphorescence is enhanced since it can borrow intensity from spin-allowed radiative singlet ($S_n \rightarrow S_0$) transitions.[49] The enhancement is proportional to the size of the matrix element of the spin–orbit coupling (SOC) of the triplet and singlet states, which is expected to lead to a more pronounced plasmonic effect on the phosphorescence.

Accurate values for SOC matrix elements, excitation energies of triplet states, and their deactivation rates are relevant for modern photophysical studies. Even without considering the plasmon effect, determinations of the rate constants of ISC and the quantum yield of phosphorescence are difficult by using experimental techniques. Modern quantum chemistry methods provide complementary information. Although, rate constants of first-order electronic transitions, such as ISC, internal conversion (IC) and fluorescence can be calculated with sufficient accuracy,[50–55] calculations of the IC and ISC rate constants are still challenging for large molecules.[56] The IC and ISC rate constants can be calculated using *ab initio* and molecular dynamics methods.[57–59] However, these approaches can mainly be applied on small molecules and they are difficult to extend to large molecules since the computational costs increase rapidly with increasing size of the molecule. Valiev *et al.* have developed computational approaches to calculate ISC and IC rate constants based on Plotnikov's time-independent formalism. We have successfully employed this method in calculations of fluorescence rate constants of molecules near plasmonic NPs.[56]

Calculations of the rate constants of second-order electronic transitions are even more difficult because it is necessary to calculate the total lifetime of the triplet state of the molecule.[49] Currently, the phosphorescence rate constant or the phosphorescence lifetime can be calculated within the framework of the quadratic response formalism at the time-dependent density functional theory (TD DFT) level using the Dalton program.[60,61] However, the phosphorescence lifetime cannot uniquely characterize the total lifetime of the triplet state, since there are also other non-radiative channels for its deactivation. The most important ones among them are the first-order physical channels namely, ISC from T_1 to S_0, reverse ISC (RISC) to S_1 and to energetically higher-lying singlet states (S_n) as well as the second-order IC process between T_1 and S_0, where the wave functions of T_1 and S_0 are not pure spin states.[62] Intermolecular quenching channels may also play an important role.[63]

The rate constants of photophysical processes including phosphorescence change when a molecule is placed in the plasmon field of NPs. The plasmon field affects the probability of radiative transitions,[56] and can also affect the rate constants of nonradiative transitions.[64,65] We are not aware of any implementation of theoretical models, which considers the plasmon field effect on the total lifetime of the molecular triplet state using computational methods that accounts for properties of the individual molecules. Here, we have developed such a computational method and applied it to the well-known xanthene dyes rhodamine 123 (**Rh123**) and 2Br-rhodamine 123 (**Rh123-2Br**). Replacing two hydrogen atoms with halogen (Br) atoms increases the SOC matrix element and the yield of the triplet state.[49] The plasmonic effects on the radiative transitions of **Rh123-2Br** is expected to be larger than for **Rh123**, even though the total quantum yield of fluorescence decreases when hydrogen atoms are replaced by the heavier Br. The plasmon effect is simulated with our model that considers the dipole–dipole interaction between the plasmonic NP and the dye molecule.[4,56]

2. Experimental and computational details

2.1 Experimental details

2.1.1 Chemicals. **Rh123** (BioReagent, HPLC) was purchased from Sigma-Aldrich. **Rh123-2Br** was synthesized in the

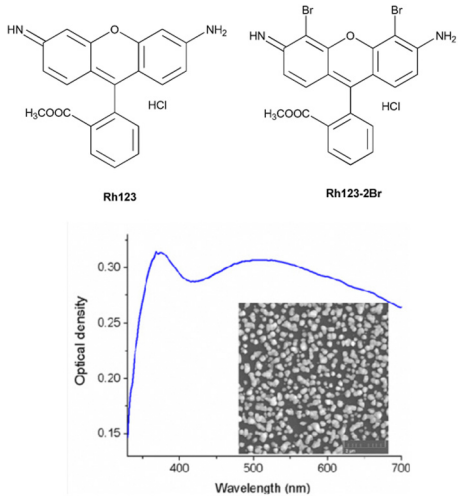

Fig. 1 The chemical structures of the studied molecules and the absorption spectrum of the SIF. The inset shows the SEM image of the synthesized SIF sample.

NIOPIK State Research Center according to the method published in ref. 66 and 67. The chemical structures and the optimized molecular structures are shown in Fig. 1 and 2, respectively.

$AgNO_3$, NaOH, NH_4OH, D-glucose, polyvinyl alcohol (PVA) of analytical purity (Sigma Aldrich) were used for the synthesis of silver island films. Ultrapure water, obtained with the Smart S15 UVF system (Drawell), was used to prepare the samples.

2.1.2 Sample preparation. A detailed description of the synthesis of silver island film (SIF) samples by the chemical deposition method has been reported in ref. 56 and 68. SEM images obtained using the Mira 3LMU microscope (Tescan) showed that the average diameter of the Ag NPs in the SIF is 94 ± 30 nm (inset in Fig. 1).[56] The synthesized films have an absorption band in the visible region of the spectrum (Fig. 1). Polymer films with a dye concentration of 5×10^{-4} mol L^{-1} were deposited over clean glasses or on the SIF surface by using a spin-coating method at 3000 rpm. The weight concentration of PVA in the solution was 5 wt%. The amount of molecules deposited on various substrates was controlled by micro-weighing the glass substrates and the SIF sample before and after deposition of the polymer film. The mass of the films was the same in both cases.

2.1.3 Details of the measurements. The absorption spectra of the samples were measured with a Cary-300 spectrophotometer (Agilent Techn.). The fluorescence spectra were obtained at steady-state excitation with an Eclipse spectrofluorimeter (Agilent Techn.). The kinetics of the fluorescence decay was recorded in the time-correlated single-photon counting mode using the TCSPC FLS1000 system (Edinburgh Instr.). The excitation of the samples was carried out with a picosecond laser (λ_{gen} = 488 nm and τ = 120 ps). The fluorescence lifetime was estimated using the Fluoracle software (Edinburgh Instr.). The intensity of fluorescence decay was obtained using (1):

$$I(t) = \sum_{i=1}^{n} \alpha_i \exp(-t/\tau_i), \quad (1)$$

where the τ_i is the lifetime of the excited state (the signal decay time), the α_i is the amplitude or fraction of the contribution of the i-th component $\left(\sum_i \alpha_i = 1.0\right)$.

Testing the quality of the fitting of the decay function (Fig. S1, ESI†) yielded a χ^2 value of 1.15.

The delayed fluorescence (DF) and phoshorescence spectra were obtained with the Eclipse spectrofluorimeter (Agilent Techn.). The intensity of the DF and phosphorescence spectra at each wavelength were recorded 300 μs after the beginning of the flash of the Xe lamp, *i.e.*, after the complete decay of the fluorescence signal. The decay kinetics of the long-lived luminescence was also recorded with the FLS1000 spectrometer (Edinburgh Instr.). The photoexcitation of the samples at λ_{exc} = 490 nm was carried out by using a laser system based on the Nd:YAG laser (LQ529) with an OPO (LP604) and a second-harmonic generator (LG305) from SolarLS. The delay in the detection of the decay of the DF and phosphorescence was 1 μs. The luminescence kinetics was also calculated using eqn (1). Assessing the fit of the decay of the DF and phosphorescence (Fig. S2, ESI†) yielded χ^2 values of 1.2 and 1.4, respectively.

The samples were evacuated with Optistat DN-V (Oxford Instr.) when measuring the long-lived luminescence. The measurements were carried out at a temperature of 293 K.

The temperature-dependent measurements were carried out by cooling the samples with liquid nitrogen and heating them with a heater built into the cryostat.

The fluorescence quantum yields (φ_{fl}) of **Rh123** and **Rh123-2Br** in ethanol solutions were determined with the AvaSphere 30-REFL integrating sphere and the AvaSpec-ULS2048 spectrometer (Avantes) using the absolute method. An LQ529 laser system with OPO second-harmonic generator was used as the source of the monochromatic light with λ_{exc} = 490 nm. The φ_{fl} value was determined using eqn (2):[69]

$$\phi_{fl} = \frac{PN(Em)}{PN(Abs)} = \frac{\int \frac{\lambda}{hc}\left[I_{em}^{sample}(\lambda) - I_{em}^{reference}(\lambda)\right]d\lambda}{\int \frac{\lambda}{hc}\left[I_{exc}^{reference}(\lambda) - I_{exc}^{sample}(\lambda)\right]d\lambda}, \quad (2)$$

where PN(Abs) is the number of absorbed photons; PN(Em) is the number of emitted photons; λ is wavelength; h is Planck's constant, c is velocity of light, I_{exc}^{sample} and $I_{exc}^{reference}$ are the integral intensity of the excitation that was recorded with and without the sample, respectively. I_{em}^{sample} and $I_{em}^{reference}$ are the

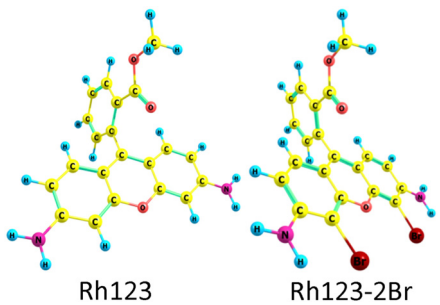

Fig. 2 Optimized molecular structures of **Rh123** and **Rh123-2Br**.

integral intensity of the emission that was recorded with and without the sample, respectively.

3. Theory and computational details

3.1. First-order electronic transitions

The rate constants of ISC (k_{ISC}), IC (k_{IC}) and radiative (k_r) electron transitions were calculated using the computational approach developed by Valiev *et al.*[70] The methods are described in detail in ref. 51, 52, 70 and 71. We present here only the most important expressions.

The k_r rate constant is calculated using the Strickler–Berg equation:[72]

$$k_r = \frac{1}{1.5}\cdot f \cdot E^2(S_1 \rightarrow S_0), \tag{3}$$

where f is the oscillator strength and $E(S_1 \rightarrow S_0)$ is de-excitation energy from S_1 to S_0.

The IC rate constants (k_{IC}) were calculated using the expression in eqn (4), which is described in detail in ref. 53,

$$k_{IC} = \frac{4}{\Gamma_f}\sum_{n_1,n_2,\ldots,n_{3N-6}}^{E_{if}=n_1\omega_1+n_2\omega_2+\ldots n_{3N-6}\omega_{3N-6}} \left(D\prod_{k=1}^{3N-6}\left(\frac{e^{-y_k}y_k^{n_k}}{n_k!}\right)^{1/2} + \left[\sum_{j=1}^{3N-6} d_j\cdot t_j \prod_{\substack{k=1\\k\neq j}}^{3N-6}\left(\frac{e^{-y_k}y_k^{n_k}}{n_k!}\right)^{1/2}\right] + \sum_j\sum_{j'} t_j b_{j'} W_{jj'}\cdot \prod_{\substack{k=1\\k\neq j\\k\neq j'}}^{3N-6}\left(\frac{e^{-y_k}y_k^{n_k}}{n_k!}\right)^{1/2}\right)^2 \tag{4}$$

where the summation considers the energy conservation condition with

$$W_{jj'} = -\sum_\nu\sum_q\sum_{\nu'}\sum_{q'}\left\langle \frac{\phi_i(\vec{r},\vec{s},\vec{R})\partial^2\phi_f(\vec{r},\vec{s},\vec{R})}{\partial R_{\nu q}R_{\nu' q'}}\right\rangle\Bigg|_{\vec{R}=\vec{R}_0} \times M_\nu^{-1/2}M_{\nu'}{}^{-1/2}L_{\nu qj}L_{\nu' q' j'}, \tag{5}$$

$$D = -\sum_\nu\sum_q (2M_\nu)^{-1}\left\langle \varphi_i(\vec{r},\vec{s},\vec{R})\left|\frac{\partial^2}{\partial R_{\nu q}{}^2}\right|\varphi_f(\vec{r},\vec{s},\vec{R})\right\rangle\Bigg|_{\vec{R}=\vec{R}_0}, \tag{6}$$

$$d_j = -\sum_\nu\sum_q M_\nu^{-1/2}L_{\nu qj}\left\langle \varphi_i(\vec{r},\vec{s},\vec{R})\frac{\partial\varphi_f(\vec{r},\vec{s},\vec{R})}{\partial R_{\nu q}}\right\rangle\Bigg|_{\vec{R}=\vec{R}_0}, \tag{7}$$

$$y_j = \frac{1}{2}(\omega_j)\cdot\left|Q_{0_j}^f - Q_{0_j}^i\right|^2, \tag{8}$$

$$W_j = \left[\sum_\nu\sum_q\left(\frac{\partial\left(H_{SO}^{if}\right)}{\partial R_{\nu q}}\Bigg|_{\vec{R}=\vec{R}_0} M_\nu^{-1/2}L_{\nu qj}\right)\right]. \tag{9}$$

Here, $\left\langle \phi_i(\vec{r},\vec{s},\vec{R})\frac{\partial\phi_f(\vec{r},\vec{s},\vec{R})}{\partial R_{\nu q}}\right\rangle\Big|_{\vec{R}=\vec{R}_0}$ and $\left\langle \frac{\phi_i(\vec{r},\vec{s},\vec{R})\partial^2\phi_f(\vec{r},\vec{s},\vec{R})}{\partial R_{\nu q}R_{\nu' q'}}\right\rangle\Big|_{\vec{R}=\vec{R}_0}$ are the nonadiabatic coupling matrix elements (NACME) of first and second order, respectively. M_ν is the mass of the νth atom, and $L_{\nu qj}$ are coefficients of the linear relation between the Cartesian (R) and the normal coordinates (Q): $R_{\nu q} - R_{0_{\nu q}} = M_\nu^{-1/2}L_{\nu qj}Q_j$; y_j is the Huang–Rhys factor of the jth vibrational mode; E_{if} is the energy difference between the initial and final states; n_j and ω_j are the excitation quantum number and the energy of the jth mode, respectively; b_j and t_j are the matrix elements of Q_j and d/dQ_j between the nuclear functions of the initial and final electronic states, which are calculated by considering anharmonic effects using the Morse potential.[51,53]

The k_{ISC} rate constant is calculated using the expression in eqn (10):

$$k_{ISC} = \frac{4}{\Gamma_f}\sum_n^{E_{if}=(\vec{n},\vec{\omega})}\left(H_{SO}^{if}\Big|_{\vec{R}=\vec{R}_0}\left[\prod_{k=1}^{3N-6}\sqrt{\frac{\exp(-y_k)y_k^{n_k}}{n_k!}}\right] + \sum_{j=1}^{3N-6} t_j W_j\left[\prod_{\substack{k=1\\k\neq j}}^{3N-6}\sqrt{\frac{\exp(-y_k)y_k^{n_k}}{n_k!}}\right]^2\right), \tag{10}$$

where W_j is given by (10):

$$W_j = \sum_{\nu,q}\frac{\partial H_{SO}^{if}}{\partial R_{\nu q}}\Big|_{\vec{R}=\vec{R}_0} M_\nu^{-1/2}L_{\nu qj} \tag{11}$$

Here, the $4/\Gamma_f$ factor is 1.6×10^9 s^{-1} cm^{-2} and H_{SO}^{if} is the matrix elements of the spin–orbit coupling operator between the initial (i) and the final (f) electronic states.

The fluorescence quantum yield (φ_{fl}) in the absence of a NP can be written as:[70,73]

$$\phi_{fl} = \frac{k_r}{k_r + k_{nr}}, \tag{12}$$

where the rate constant of the nonradiative transition (k_{nr}) is the sum of the ISC rate constants ($\sum k_{ISC}(S_1 \rightarrow T_n)$) from the lowest excited singlet state (S_1) to the energetically lower-lying triplet states (T_n) and the IC rate constant from S_1 to the singlet ground state (S_0) ($k_{IC}(S_1 \rightarrow S_0)$).[73,74] The $\sum k_{ISC}(S_1 \rightarrow T_n)$, $k_{IC}(S_1 \rightarrow S_0)$ and $k_r(S_1 \rightarrow S_0)$ rate constants were calculated as described in ref. 51, 70 and 71.

Reversed ISC from T_1 to S_1 is calculated using eqn (13)[75]

$$k_{RISC}(T_1 \rightarrow S_1) = k_{ISC}(S_1 \rightarrow T_1)\cdot\frac{\exp\left(-E_{S_1T_1}/kT\right)}{3}. \tag{13}$$

A similar expression is used for the reverse IC (RIC) from T_1 to T_2:

$$k_{RIC}(T_1 \rightarrow T_2) = k_{IC}(T_2 \rightarrow T_1)\cdot\frac{\exp\left(-E_{T_2T_1}/kT\right)}{6}, \tag{14}$$

where T is temperature (in K) and k is Boltzmann's constant.

3.2. Second order electron transitions

The spin-mixed wave functions of the S_0 and T_1 states can be obtained using perturbation theory.[49] The spin-mixed triplet state in eqn (15) and the spin-mixed singlet state in eqn (16) are obtained by adding contributions from states of the other spin multiplicity. The mixing coefficients are obtained by using the perturbation theory expressions in eqn (17) and (18).

$$\psi(\tilde{T}_1) = \psi(T_1) + \sum a_p \psi(S_p), \tag{15}$$

$$\psi(\tilde{S}_0) = \psi(S_0) + \sum b_m \psi(T_m), \tag{16}$$

$$a_p = \frac{\langle \psi(T_1)|\hat{H}_{SO}|\psi(S_p)\rangle}{E(T_1) - E(S_p)}, \tag{17}$$

$$b_m = \frac{\langle \psi(S_0)|\hat{H}_{SO}|\psi(T_m)\rangle}{E(S_0) - E(T_m)}. \tag{18}$$

The phosphorescence rate constant (k_{phos}) is then given by

$$k_{phos}(\tilde{T}_1 \rightarrow \tilde{S}_0) = \sum_p k_r(S_p \rightarrow S_0)|a_p|^2 \left(\frac{E(T_1)}{E(S_p)}\right)^3 + \sum_m |b_m|^2 k_r^m(T_m \rightarrow T_1)\left(\frac{E(T_1)}{E(T_1) - E(T_m)}\right)^3 \tag{19}$$

The expression in eqn (19) shows that the triplet contributions decrease the phosphorescence rate constant (k_{phos}) and the singlet contributions increase it.

An analogous expression involving the NACME is used when calculating the rate constant for IC between the spin-mixed T_1 and S_0 states.

$$\left\langle \psi(\tilde{T}_1)|\hat{A}|\psi(\tilde{S}_0)\right\rangle = \sum_m b_m \langle \psi(T_1)|\hat{A}|\psi(T_m)\rangle + \sum_p a_p \langle \psi(S_p)|\hat{A}|\psi(S_0)\rangle \tag{20}$$

The $\langle \psi(T_1)|\hat{A}|\psi(T_m)\rangle$ and $\langle \psi(S_p)|\hat{A}|\psi(S_0)\rangle$ matrix elements are needed when calculating $\langle \psi(\tilde{T}_1)|\hat{A}|\psi(\tilde{S}_0)\rangle$. Calculations of these matrix elements are difficult and require the $L_{\nu qj}$ matrix for all electronic states. The determination of $\breve{k}_{IC}(\tilde{T}_1 \rightarrow \tilde{S}_0)$ using $E(T_1) - E(S_0)$ and vibronic factors is not trivial.[51]

However, the X–H (where X is C, N or O) bond approximation can be used, where the X–H bonds are the main accepting modes of the IC process.[51,76] This approximation is supported by experimental and computational studies showing that deuteration of X–H bonds decreases the IC probability.[77,78] The X–H bond approximation avoids explicit calculations of $\langle \psi(T_1)|\hat{A}|\psi(T_m)\rangle$ and $\langle \psi(S_p)|\hat{A}|\psi(S_0)\rangle$, since they are approximated with contributions from X–H bond. In the X–H bond approximation, $\breve{k}_{IC}(\tilde{T}_1 \rightarrow \tilde{S}_0)$ can be written as:

$$\breve{k}_{IC}(\tilde{T}_1 \rightarrow \tilde{S}_0) = \frac{\left\langle \psi(\tilde{T}_1)|\hat{A}|\psi(\tilde{S}_0)\right\rangle^2}{E_{T_1S_0}{}^2} \times Q_{T_1S_0} = \frac{1.6 \times 10^9 \times N_{XH} \times 6.25 \times 10^6 \times e^{-E_{T_1S_0}/2.17}}{E_{T_1S_0}{}^2} \times \left\langle \psi(\tilde{T}_1)|\hat{A}|\psi(\tilde{S}_0)\right\rangle^2. \tag{21}$$

where $\langle \psi(T_1)|\hat{A}|\psi(T_m)\rangle$ and $\langle \psi(S_p)|\hat{A}|\psi(S_0)\rangle$ are calculated as:[51]

$$\left\langle \psi_p\middle|\hat{A}\middle|\psi_q\right\rangle^2 = \left[\sum_{\alpha=1}^{N_{XH}} P_\alpha{}^2\right] \times \frac{N_{XH} \times 6.25 \times 10^6 \times e^{-E_{pq}/2.17}}{E_{pq}{}^2} \tag{22}$$

with the electronic factor

$$P_\alpha{}^2 = 0.01\left|\sum_{iabkk'} A_{ia}^p A_{ib}^q c_a^k c_b^{k'} + \sum_{ijakk'} A_{ia}^p A_{ja}^q c_i^k c_j^{k'}\right|_\alpha^2 \tag{23}$$

for X–H bond α. Here c_i^k, $c_j^{k'}$, c_a^k, $c_b^{k'}$, are the molecular orbital (MO) coefficients and A_{ia}^p, A_{jb}^q are configurationally interaction coefficients. The a, b indices denote virtual MO and i, j are indices of the occupied MOs. The N_{XH} is the number of X–H bonds.

Valiev *et al.* showed that for molecules with an energitically low-lying T_1 state (below 12 000 cm^{-1}), the $\breve{k}_{IC}(\tilde{T}_1 \rightarrow \tilde{S}_0)$ process determines the total lifetime of the T_1 state.[62,70]

The $\breve{k}_{IC}(\tilde{T}_1 \rightarrow \tilde{S}_0)$, $k_{phos}(\tilde{T}_1 \rightarrow \tilde{S}_0)$, $k_{RISC}(T_1 \rightarrow S_n)$ and $k_{RIC}(T_1 \rightarrow T_n)$ rate constants determine the total lifetime of the T_1 state when neglecting intermolecular processes. The phosphorescence quantum yield (φ_{phos}) can be written as

$$\phi_{phos} = \frac{k_{phos}(\tilde{T}_1 \rightarrow \tilde{S}_0)}{k_{phos}(\tilde{T}_1 \rightarrow \tilde{S}_0) + \breve{k}_{IC}(\tilde{T}_1 \rightarrow \tilde{S}_0) + k_{RISC}(T_1 \rightarrow S_n) + k_{RIC}(T_1 \rightarrow T_n)} \tag{24}$$

3.3. Intermolecular rate constants of molecules near NP surfaces

When a molecule is near a plasmonic NP, its photophysical properties change because the rate constants of the electronic transitions are affected and other intermolecular deactivation channels of the excited electronic states appear. In the dipole–dipole approximation of the interaction between the molecule and the plasmonic NP, changes in k_r can be described using the dyadic Green's function.[1,79,80] The $k_{IC}(S_1 \rightarrow S_0)$ rate constant can also change.[64] Expressions describing such changes can be derived using second-order perturbation theory, where NACME and $\vec{p}$ or only $\vec{p}$ is the perturbation operator.[64,65] $\vec{p}$ is the electric dipole transition moment. Changes in the IC rate constant can

be more than one order of magnitude but occur only at very strong electrical fields of 10^9–10^{11} V m^{-1}, whereas changes in the $k_{ISC}(S_1 \rightarrow T_1)$ rate constant occur only when the molecule is very close to the NP surface. The increase in the $k_{ISC}(S_1 \rightarrow T_1)$ rate constant is due to changes in the SOC, which is caused by heavy atoms in the NP. However, the excitation energy transfer from the molecule to the NP is much faster than ISC implying that the ISC process can be neclected.

An external electric field induces a dipole moment ($\vec{P}(\omega)$) in the NP, whose strength is $\vec{E}_0(\omega)$. The induced dipole moment $\vec{P}(\omega)$ is obtained from the polarizability ($\overleftrightarrow{\alpha}(\omega)$) of the NP and the strength of the electric field as $\vec{P}(\omega) = \overleftrightarrow{\alpha}(\omega).\vec{E}_0(\omega)$. The frequency-dependent polarizability $\overleftrightarrow{\alpha}(\omega)$ can be estimated by using Sommerfeld–Drude theory:[81–85]

$$\alpha(\omega) = \frac{\varepsilon(\omega) - \varepsilon_m}{\varepsilon(\omega) + 2\varepsilon_m} {R_{NP}}^3, \tag{25}$$

where

$$\varepsilon(\omega) = 1 - \frac{{\omega_{pl}}^2}{\omega^2 + i\omega\gamma}. \tag{26}$$

ω is the angular frequency (in Hz); γ is the damping (or electron-collision) rate constant (in s^{-1}), $\omega_{pl} = 4\pi n_0 e^2/m^*$ is the plasma frequency of the free-electron gas, e is electron charge, n_0 is the concentration of free electrons in per unit (m^{-3}); m^* is the effective mass of the electron, and ε_m is dielectric permittivity of the media surrounding the NP.

When the molecule is near the NP, the total electric field strength can be written as:

$$\vec{E}(\omega) = \vec{E}_0(\omega) + \overleftrightarrow{G}(\vec{r}) \cdot \overleftrightarrow{\alpha}(\omega) \cdot \vec{E}_0(\omega), \tag{27}$$

Where $\overleftrightarrow{G}(\vec{r})$is the dyadic Green's function that in the electric dipole–dipole approximation is given by:

$$\overleftrightarrow{G}(\vec{r}) = -\frac{1}{r^3}\left(\overleftrightarrow{I} - 3\frac{\vec{r} \times \vec{r}}{r^2}\right), \tag{28}$$

where $\overleftrightarrow{I}$ is the unit dyadic tensor. When the total electric field ($\vec{E}$) of the molecule–NP system is known, the plasmon-affected radiative rate constant $k'(\vec{r})$ can be expressed as:[1,56,80]

$$\begin{aligned} k'_r &= \frac{4\omega^3}{3c^3\hbar}\left|\vec{p} \cdot \vec{E}\right|^2 \\ &= \left[\vec{p}^2 + \vec{p}\left|\overleftrightarrow{\alpha}(\omega)\overleftrightarrow{\mathbf{G}}(\mathbf{r})\right|^2 \vec{p} + 2\mathrm{Re}\vec{p}\left(\overleftrightarrow{\alpha}(\omega)\overleftrightarrow{\mathbf{G}}(\mathbf{r})\right)\vec{p}\right], \end{aligned} \tag{29}$$

where $\vec{p}$ is the electric dipole transition moment. Thus, the plasmon-affected radiative rate constant $k'(\vec{r})$ consists of three terms, where the first one is k_r *i.e.*, the rate constant in the absence of the NP, the second term depends on $1/d^6$ and the third cross term can be positive or negative and depends on $1/d^3$, where d is the distance between the molecule and the NP.

The changes in k_r affect $k'_{phos}\left(\tilde{T}_1 \rightarrow \tilde{S}_0\right)$ in eqn (19) and make the rate constant also dependent on d. The energy transfer occurs when the molecule is near the NP. We recently showed that the $k_{transfer}$ rate constant from S_1 to the NP can for short distances be written as:[56]

$$k_{transfer} = \frac{\vec{p}^2}{\hbar c^3 2 \cdot (d)^3} \cdot \mathrm{Im}\left(\frac{\varepsilon(\omega) - 1}{\varepsilon(\omega) + 1}\right), \tag{30}$$

where p is the transition dipole moment ($\langle\langle\psi(S_1)|\vec{p}|\psi(S_0)\rangle\rangle$). The $k_{transfer}$ rate constant can generally be written as:[1,4,79,80]

$$k_{transfer} = \frac{1}{2\hbar} \cdot \mathrm{Im}\left(\vec{p}\overleftrightarrow{\mathbf{G}}(\mathbf{r})\overleftrightarrow{\alpha}(\omega)\overleftrightarrow{\mathbf{G}}(\mathbf{r})\vec{p}\right), \tag{31}$$

where $k_{transfer}$ has for large d a $1/d^6$ dependency, which is the same as for the Förster resonance-energy-transfer mechanism. For the plasmon-enhanced radiative rate constant $k'(\vec{r})$ in eqn (31), there are two terms whose distance dependency are $1/d^3$ and $1/d^6$, respectively, which can be combined to one $k_{transfer}(S_1)$.

The $k_{transfer}(S_1)$ rate constant given by eqn (30) and (31) can be easily transformed into $k_{transfer}(T_1)$ by replacing p with $\vec{p}'' = \left\langle\psi(\tilde{T}_1)|\vec{p}''|\psi(\tilde{S}_0)\right\rangle$ in eqn (30) and (31). The rate constant for the energy transfer from the T_1 state of the molecule to the NP and the corresponding quantum yield can then be calculated.

The expression for the phosphorescence quantum yield of a molecule near a NP is then:

$$\begin{aligned} \phi'_{phos} &= \frac{k'_{phos}\left(\tilde{T}_1 \rightarrow \tilde{S}_0\right)}{k'_{phos}\left(\tilde{T}_1 \rightarrow \tilde{S}_0\right) + k_{IC}\left(\tilde{T}_1 \rightarrow \tilde{S}_0\right) + k_{RISC}(T_1 \rightarrow S_n)} \\ &\quad \times \frac{1}{k_{RIC}(T_1 \rightarrow T_n) + k_{transfer}(T_1)}. \end{aligned} \tag{32}$$

The $k_{IC}(S_1 \rightarrow S_0)$ rate constant can also increase due to the external electric field[64,65] leading to the changes in $\check{k}_{IC}(\tilde{T}_1 \rightarrow \tilde{S}_0)$. In this work, we have estimated this effect on **Rh123** and **Rh123-2Br**. In the experimental studies, we use a laser with power of 0.004 W and a cross section of the beam of 0.0785 cm^2 yielding an electric field of 10^7 V m^{-1}. We estimate the plasmon enhancement effect on the external electric field using eqn (27). The total external field can reach 8×10^7 V m^{-1} when the distance is 2–9 nm between the molecule and the NP. However, this electric field is still too weak to significantly increase the $k_{IC}(S_1 \rightarrow S_0)$ rate constant, at least for the studied molecules. Calculations of the induced effect on $k_{IC}(S_1 \rightarrow S_0)$ show that the rate constant change by more than one order of magnitude when the electric field is 5×10^8 V m^{-1} and 10^{10} V m^{-1} for **Rh123-2Br** and **Rh123**, respectively.

We used the X–H approximation in the calculation of the changes in $k_{IC}(S_1 \rightarrow S_0)$ that are induced by the electric field. The $\hat{\Lambda} + \vec{p}$ (NACME + $\vec{p}$) operator is used as the perturbation operator in the second-order perturbation theory expression.[64] Thus, we neglect changes in $k_{IC}(S_1 \rightarrow S_0)$ and in $\check{k}_{IC}(\tilde{T}_1 \rightarrow \tilde{S}_0)$.

The employed parameters of the spherical silver NP are: R_{NP} = 47.3 nm, ε_m = 3.5, $\gamma = 2.5 \times 10^{13}$ s^{-1}, and $n_0 = 5.78 \times 10^{13}$ m^{-3}. The molecular parameters are calculated using quantum chemical methods as described in the next section.

3.4. Computational details

The optimization of the molecular structures (shown in Fig. 2), calculations of the second derivatives of the potential energy surface (Hessian) of the singlet and triplet states, and calculations of the NACME were performed at the DFT and TD DFT levels for the ground and excited states using the MN15 functional and the 6-31G(d,p) basis set. The calculations were done with Gaussian 16.[86] However, energetically higher-lying electronic states with other spin multiplicities, spin–orbit coupling matrix elements (SOCME) and $\left\langle \psi(\tilde{T}_n)|\vec{p}''|\psi(\tilde{S}_m)\right\rangle$ between them were calculated at the extended multi-configuration quasi-degenerate perturbation theory of second order (XMC-QDPT2)[87] level of theory using GAMESS-US.[88] We used the XMC-QDPT2 method to ensure that we get accurate energies of the singlet and triplet states, which is important when calculating rate constants. The accuracy of the excitation energies calculated at the TDDFT level is usually not enough for this purpose. $\langle\psi(T_1)|\hat{A}|\psi(T_m)\rangle$, $\langle\psi(S_p)|\hat{A}|\psi(S_0)\rangle$, $E(T_1) - E(S_p)$, $E(S_0) - E(T_m)$, $\langle\psi(S_1)|\vec{p}|\psi(S_0)\rangle$, and $\left\langle \psi(\tilde{T}_n)|\vec{p}''|\psi(\tilde{S}_m)\right\rangle$ were therefore calculated for 50 singlet and 50 triplet states at the XMC-QDPT2/6-31G(d,p) level using an active space with 12 electrons in 12 orbitals. The largest contributions to the $\check{k}_{IC}(\tilde{T}_1 \rightarrow \tilde{S}_0)$ and $k_{phos}(\tilde{T}_1 \rightarrow \tilde{S}_0)$ rate constants of **Rh123** and **Rh123-2Br** originate from the $S_1 \rightarrow S_0$ and $S_1 \rightarrow T_1$ transitions. For these molecules, it is enough to consider only S_1 and T_1 when calculating $\check{k}_{IC}(\tilde{T}_1 \rightarrow \tilde{S}_0)$ and $k_{phos}(\tilde{T}_1 \rightarrow \tilde{S}_0)$ using eqn (19) and (21). However, for other molecules, it might be necessary to calculate many singlet and triplet states to obtain accurate rate constants.

4. Results and discussion

4.1. Photophysical properties in the absence of plasmonic NPs

The normalized absorption and fluorescence spectra or **Rh123** and **Rh123-2Br** in polymer films are shown in Fig. 3(a). The molecules absorb between 400 and 650 nm.

The maximum of the absorption spectrum (λ_{abs}^{max}) of **Rh123** is at 510 nm, and the fluorescence maximum (λ_{fl}^{max}) is at 535 nm. The absorption and fluorescence spectra of its brominated analog are slightly red shifted with the maximum of the absorption and fluorescence band at 515 nm and 540 nm, respectively. The fluorescence lifetime that is estimated from the decay rate is τ_{fl} = 3.48 ± 0.05 ns for **Rh123** and τ_{fl} = 2.10 ± 0.05 ns for **Rh123-2Br**.

There are two bands in the spectrum of the long-lived luminescence of the dye film (Fig. 3(b)). The position and maximum of the first luminescence band coincides with the maximum of the fast fluorescence and is due to delayed fluorescence (DF), whereas the wide band with a maximum at ~680 nm is due to phosphorescence.

The DF and the phosphorescence decay exponentially with a single exponent. The DF lifetime (τ_{DF}) is shorter than the one for the phosphorescence (τ_{phos}). The phosphorescence of **Rh123-2Br** is stronger than for **Rh123**. The I_{DF}/I_{phos} intensity ratio for **Rh123-2Br** is 3.6 and 2.6 for **Rh123**. The intensity of the long-lived luminescence of **Rh123-2Br** is almost an order of magnitude higher than for **Rh123**. The luminescence lifetime is shorter for **Rh123-2Br** than for **Rh123** (Table 1). The shorter fluorescence lifetime of **Rh123-2Br** is due to a faster decay of the S_1 state. It decays not only to S_0 but also to the T_1 state due to the larger ISC rate constant caused by the heavy atom effect of Br.[49] The shorter DF and phosphorescence lifetimes of **Rh123-2Br** is due to the faster decay rate of the T_1 state to both S_0 and S_1 because of the stronger SOC of the brominated chromophore.

The triplet character of the long-lived luminescence was confirmed by temperature measurements and by quenching with molecular oxygen. The emission bands were quenched when injecting air into the evacuated chamber of the cryostat. The phosphorescence intensity decreased when the films were heated to 360 K. The DF, which is a result of the RISC from T_1 to S_1, has the opposite behaviour (Fig. 4). The Boltzmann population of the vibrational levels of the T_1 state leads to stronger DF intensity and quenched phosphorescence when increasing temperature.

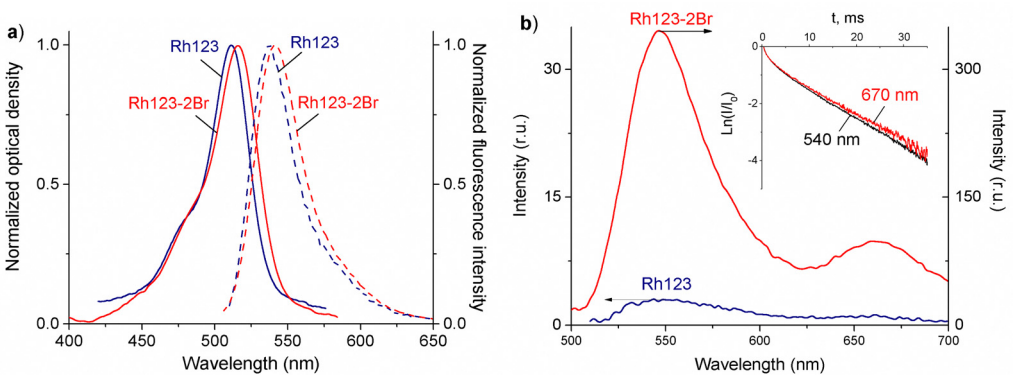

Fig. 3 (a) Normalized absorption (solid curves) and fluorescence (dashed curves, λ_{exc} = 490 nm) spectra and (b) the DF and phosphorescence (long-lived luminescence) spectra of **Rh123** and **Rh123-2Br** in PVA films at T = 293 K. Inset: The decay rate of the DF measured at λ_{reg} = 540 nm, which is near the fluorescence maximum, and at λ_{reg} = 670 nm, which is near the phosphorescence maximum of **Rh123-2Br**. The different fluorescence and delayed luminescence intensities of **Rh123** is due to the larger quantum yield of fluorescence (φ_{fl}) of 84% as compared to the quantum yield of phosphorescence (φ_{ph}) of 16%.

Table 1 Spectral-luminescent parameters of **Rh123** and **Rh123-2Br** in PVA films

Dye	λ_{abs}^{max}, nm	λ_{fl}^{max}, nm	τ_{fl}, ns	φ_{fl}	τ_{DF}, ms	τ_{phos}, ms
Rh123	510	535	3.48 ± 0.05	0.84	9.8 ± 0.3	13.6 ± 0.3
Rh123-2Br	515	540	2.10 ± 0.05	0.40	6.3 ± 0.3	7.5 ± 0.3

The obtained data indicate that triplet states are formed upon photoexcitation of the rhodamine films due to a fast singlet–triplet ISC transition. The triplet state decays through direct radiative transition (phosphorescence with an energy of $h\nu_{phos}$) and reverse ISC from T_1 to S_1, which is followed by delayed fluorescence emission with an energy of $h\nu_{DF}$. Since the phosphorescence efficiency is proportional to the number of molecules in the T_1 state, its lifetime should be about the same as the radiative lifetime of S_1.

However, the ratio between the two relaxation pathways is difficult to measure, which suggests that triplet–triplet annihilation may also contribute to the DF. This process occurs when the concentration of rhodamine is sufficiently high in the polymer film.

The calculated energy levels of the S_1 and T_1 states of the molecule (Table 2) correlate well with experimental data for the $S_1 \rightarrow S_0$ and $T_1 \rightarrow S_0$ transitions (Table 1). The discrepancy between the calculated and experimental energies of the S_1 state is smaller than 0.1 eV, and for the T_1 state it is 0.2 eV. Only one triplet (T_1) lies below the S_1 state. The energy difference between the S_1 and T_1 states (ΔE_{ST}) is 2661 and 1855 cm^{-1} for **Rh123** and **Rh123-2Br**, respectively. The $k_{ISC}(S_1 \rightarrow T_1)$ rate constant for **Rh123-2Br** is two orders of magnitude larger than for **Rh123** since the $\langle S_1|H_{SO}|T_1\rangle$ matrix element for the brominated molecule is almost twice the one for **Rh123**. The $\langle T_1|H_{SO}|S_0\rangle$ matrix element of **Rh123-2Br** is three times larger than for **Rh123**. Reverse ISC from T_1 to S_1 does not affect the total lifetime of T_1 because the energy difference between the two states is too large for reverse ISC.

The phosphorescence rate constants $k_{phos}(\tilde{T}_1 \rightarrow \tilde{S}_0)$ estimated using eqn (19) are 1.2 and 1.5 s^{-1} for **Rh123** and **Rh123-2Br**, respectively, which correspond to lifetimes of 833 and 666 ms. Since the typical lifetime of the T_1 state of organic molecules is in the millisecond range, the phosphorescence is not the only relaxation pathway of the T_1 state.

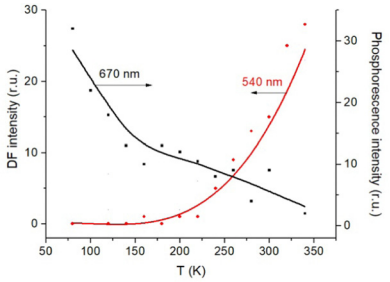

Fig. 4 Temperature dependence of the DF and phosphorescence of **Rh123-2Br** in the polymer film.

Table 2 Calculated and experimental values (in parenthesis) of the excitation energies, spin–orbit coupling matrix elements ($\langle S_1|H_{so}|T_1\rangle$ and $\langle T_1|H_{so}|S_0\rangle$), rate constants of the photophysical processes, and the quantum yields of fluorescence ($\varphi_{fl}(S_1 \rightarrow S_0)$) and phosphorescence ($\varphi_{phos}(\tilde{T}_1 \rightarrow \tilde{S}_0)$) of the studied molecules

	Rh123	**Rh123-2Br**
S_1, eV	2.37 (2.32)	2.20 (2.30)
T_1, eV	2.04 (1.86)	1.97 (1.85)
$\langle S_1\|H_{SO}\|T_1\rangle$, cm^{-1}	0.26	0.55
$\langle T_1\|H_{SO}\|S_0\rangle$, cm^{-1}	0.33	1.09
$k_{ISC}(S_1 \rightarrow T_1)$, s^{-1}	5×10^6	1×10^7
$k_{IC}(S_1 \rightarrow S_0)$, s^{-1}	2×10^7	8×10^7
$k_r(S_1 \rightarrow S_0)$, s^{-1}	2×10^8 (2.4×10^8)	1×10^8 (1.9×10^8)
$\varphi_{fl}(S_1 \rightarrow S_0)$, s^{-1}	0.90 (0.84)	0.55 (0.40)
$k_{ISC}(T_1 \rightarrow S_0)$, s^{-1}	3×10^{-7}	3×10^{-6}
$k_{phos}(\tilde{T}_1 \rightarrow \tilde{S}_0)$, s^{-1}	1.2 (1.2)	1.5 (1.04×10^2)
$k_{RISC}(T_1 \rightarrow S_1)$, s^{-1}	5	5×10^2
$k_{IC}(\tilde{T}_1 \rightarrow \tilde{S}_0)$, s^{-1}	5×10^{-3}	1×10^{-1}
$k_{RIC}(T_1 \rightarrow T_2)$, s^{-1}	1×10^{-9}	90
$\varphi_{phos}(\tilde{T}_1 \rightarrow \tilde{S}_0)$, s^{-1}	0.23	0.002

The calculated rate constants of the reverse ISC ($k_{RISC}(T_1 \rightarrow S_1)$) at room temperature are 5 and 5×10^2 s^{-1} for **Rh123** and **Rh123-2Br**, respectively. At 80 K, these processes cannot determine the total lifetime of the T_1 state due to the slow reverse ISC transition from T_1 to S_1. When $\Delta E_{ST} < 1000$ cm^{-1}, thermally activated DF can occur thanks to a fast reverse ISC from T_1 to S_1,[75,89–92] which is also observed in the present measurements.

The calculations show that T_2 lies above S_1 for both molecules. For **Rh123-2Br**, the reverse IC transfer from T_1 to T_2 is also possible with a rate constant of $k_{RISC}(T_1 \rightarrow T_2) \sim 90$ s^{-1}. The reverse IC is an additional deactivation channel of the T_1 state. The most significant photophysical processes for **Rh123** and **Rh123-2Br** with corresponding rate constants and the energy of the involved states are shown in Fig. 5.

The rate constants of the radiative decay of S_1 as well as the calculated values of $\varphi_{fl}(S_1 \rightarrow S_0)$ agree well with the ones estimated from the ratio between the measured fluorescence quantum yield and the fluorescence lifetime of rhodamine dyes using eqn (33):[89]

$$k_r = \frac{\phi_{fl}}{\tau_{fl}} \quad (33)$$

The $T_1 \rightarrow S_1$ RISC process is main deactivation channel of the T_1 state at room temperature. The $k_{RISC}(T_1 \rightarrow S_1)$ rate constant depends strongly on ΔE_{ST}. The quantum yield of phosphorescence ($\varphi_{phos}(\tilde{T}_1 \rightarrow \tilde{S}_0)$) of **Rh123-2Br** is therefore smaller than for **Rh123**. The experimental $\varphi_{phos}(\tilde{T}_1 \rightarrow \tilde{S}_0)$ values are not known. The calculated total lifetime of the T_1 state ($\tau_{calc}(T_1)$) is 1 ms for **Rh123-2Br** and for **Rh123** it is 192 ms, which can be compared to the measured ones of 7.5 ms and 13.5 ms for **Rh123-2Br** and **Rh123**, respectively. $\tau_{calc}(T_1)$ of **Rh123-2Br** is 7.5 times smaller than the experimental value, whereas for **Rh123**, the calculated total lifetime of T_1 is 14 times larger than the measured one.

The calculated $\tau_{calc}(T_1)$ for **Rh123-2Br** is slightly shorter than the experimental value because the calculations underestimate

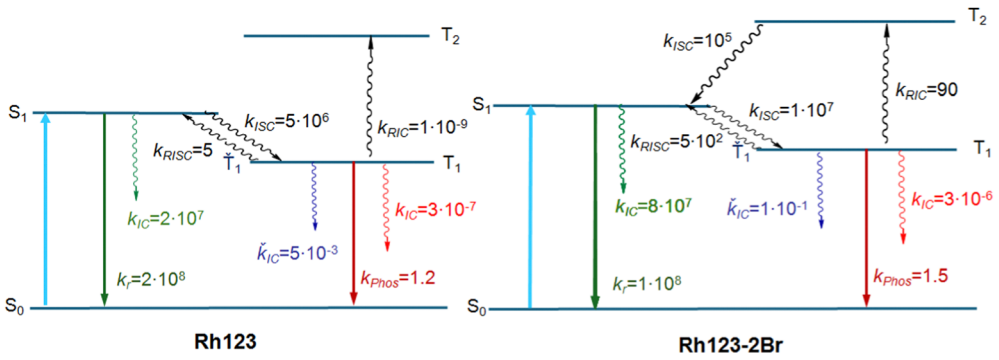

Fig. 5 The Jablonsky diagram of **Rh123** and **Rh123-2Br**.

ΔE_{ST} leading to a $k_{RISC}(T_1 \rightarrow S_1)$ rate constant that is too large. The uncertainty of the calculated ΔE_{ST} values does usually not exceed 0.1 eV (800 cm^{-1}).[70] Such an uncertainty in the ΔE_{ST} of 1800 ± 800 cm^{-1} affects the $k_{ISC}(S_1 \rightarrow T_1)$ rate constant by less than an order of magnitude, whereas due to the Boltzmann factor this uncertainty in ΔE_{ST} leads to an uncertainty of more than two orders of magnitude in the $k_{RISC}(T_1 \rightarrow S_1)$ rate constant for **Rh123-2Br**. For **Rh123**, the uncertainty in ΔE_{ST} of 2661 ± 800 cm^{-1} leads to a large uncertainty in $k_{RISC}(T_1 \rightarrow S_1)$. The rate constant can vary between 10^{-1} and 10^2 s^{-1}. The same holds for $k_{RIC}(T_1 \rightarrow T_2)$. Thus, calculations of the total rate constant for T_1 can lead to an uncertainty of two to three orders of magnitude because some of the individual relaxation channels depend on the Boltzmann factors that depend strongly on ΔE_{ST}.

The $k_{IC}(\tilde{T}_1 \rightarrow \tilde{S}_0)$ rate constant does not affect the total lifetime of T_1 since the $k_{IC}(\tilde{T}_1 \rightarrow \tilde{S}_0)$ transition is the main decay channel of the T_1 state only when $E(T_1 \rightarrow S_0)$ is less than 12 000 cm^{-1}.[62,70] The triplet de-excitation energies of **Rh123-2Br** and **Rh123** are larger than 15 000 cm^{-1}. The $k_{IC}(\tilde{T}_1 \rightarrow \tilde{S}_0)$ rate constant depends in the same way as $k_{IC}(S_1 \rightarrow S_0)$ on the energy difference between the two states. The calculations suggest that this channel determines the total lifetime of T_1 when its de-excitation energy is less than 12 000 cm^{-1}, which will be assessed in a future study.

4.2. Plasmon effect on the luminescence of Rh123 and Rh123-2Br

Measurements show that the shape and position of the absorption and fluorescence bands do not change in the presence of plasmonic NPs. Significant changes in the optical density was not registered either. However, in the presence of plasmonic NPs, the intensity of all kinds of light emission from **Rh123** and **Rh123-2Br** significantly increases (Table 3 and Fig. 6).

The plasmon enhancement factor of the fluorescence of 4.7 and 5.6 is almost the same for **Rh123** and **Rh123-2Br**, respectively. The enhancement is due to the increase in the rate constant of the radiative decay (k_r) of the S_1 state (Table 4).[56]

The change in the DF and phosphorescence intensity due to the plasmon effect was estimated by integrating the decay curves. The decay of the DF and phosphorescence was measured at 540 nm and 670 nm, respectively.

Table 3 Changes in the relative intensity of fluorescence (I_{fl}, λ_{reg} = 540 nm), DF (I_{DF}, λ_{reg} = 540 nm) and phosphorescence (I_{phos}, λ_{reg} = 670 nm), as well as their corresponding lifetimes (τ_{fl}, τ_{DF}, τ_{phos} in ms) of **Rh123** and **Rh123-2Br** in polymer films due to the plasmon effect

Dye	$\tau_{fl}^{SIF}/\tau_{fl}^{glass}$	$\tau_{DF}^{SIF}/\tau_{DF}^{glass}$	$\tau_{phos}^{SIF}/\tau_{phos}^{glass}$
Intensities			
Rh123	4.7	3.8	3.5
Rh123-2Br	5.6	5.4	8.2
	$\tau_{fl}^{SIF}/\tau_{fl}^{glass}$	$\tau_{DF}^{SIF}/\tau_{DF}^{glass}$	$\tau_{phos}^{SIF}/\tau_{phos}^{glass}$
Lifetimes			
Rh123	0.89	0.70	0.74
Rh123-2Br	1.00	1.00	1.00

The enhancement factor of the DF and the phosphorescence for **Rh123-2Br** is larger than for **Rh123**. The enhancement factor of the phosphorescence intensity for **Rh123-2Br** is larger than for the DF. The difference is probably due to the fact that DF is a two-step process and the luminescence originates from the $S_1 \rightarrow S_0$ transition as fluorescence. The lifetime of all kinds of luminescence for **Rh123** decreases on the surface of the SIF, whereas they are practically unaffected for **Rh123-2Br**.

The experimental studies show that the plasmon effect is more pronounced for **Rh123-2Br** than for **Rh123** because the intensity-borrowing effect of the $T_1 \rightarrow S_0$ transition from the $S_n \rightarrow S_0$ transitions is larger for molecules containing heavy atoms (Br).[49] The calculated $k'_{phos}\left(\tilde{T}_1 \rightarrow \tilde{S}_0\right)$ and $\varphi_{phos}(\tilde{T}_1 \rightarrow \tilde{S}_0)$ as a function of the distance between the molecule and the NP surface in Fig. 7 shows that the rate constant of phosphorescence and the quantum yield depend on the distance between the molecule and the plasmonic NP. The $k'_{phos}\left(\tilde{T}_1 \rightarrow \tilde{S}_0\right)$ rate constant for **Rh123** increases 12.7 times and for **Rh123-2Br** the phosphorescence is 26.1 times faster in the presence of the NP. At a molecular distance of 10 nm from the surface of the silver NP, the enhancement of the phosphorescence rate constant is a factor of two smaller than when the molecule is close to the NP. The changes in the calculated $k_{phos}(\tilde{T}_1 \rightarrow \tilde{S}_0)$ values due to the plasmonic NPs correlate with the measured plasmon effect on the phosphorescence rate constants.

The largest ϕ'_{phos} value is obtained for **Rh123** when the molecule is 4 nm from the NP and for **Rh123-2Br** the maximum

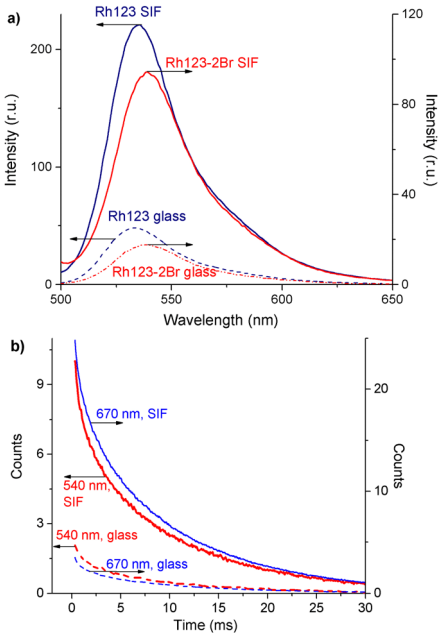

Fig. 6 (a) Fluorescence spectra of **Rh123** and **Rh123-2Br** on the glass and SIF surfaces; (b) the time-dependence of the DF (λ_{reg} = 540 nm) and phosphorescence (λ_{reg} = 670 nm) decay of **Rh123-2Br** on the glass and SIF surfaces.

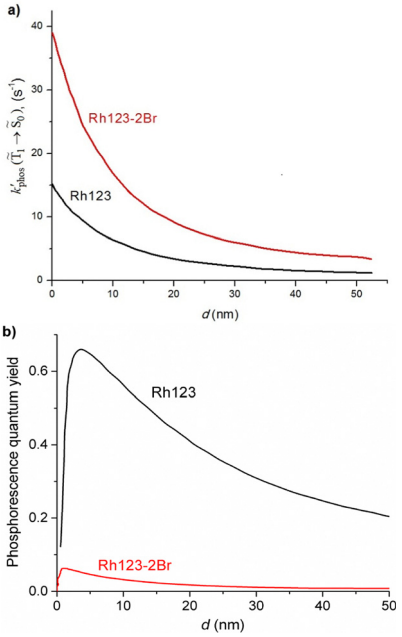

Fig. 7 The dependence of $k'_{phos}\left(\tilde{T}_1 \rightarrow \tilde{S}_0\right)$ and $\phi'_{phos}\left(\tilde{T}_1 \rightarrow \tilde{S}_0\right)$ on the distance to the surface of the Ag NP.

is at a distance of 2 nm (see Fig. 7(b)). At the maximum, the ϕ'_{phos} value of **Rh123-2Br** is 32 times larger than in the absense of the NP and for **Rh123** the maximum enhancement factor of the NP is 2.9.

At the distance for the largest enhancement factor, the $k'_{phos}\left(\tilde{T}_1 \rightarrow \tilde{S}_0\right)$ rate constant is for **Rh123-2Br** 30 times larger than without the NP and for **Rh123** the rate constant is 10 times larger. The calculated rate constants agree with those obtained experimentally (see Table 4). The plasmon effect on the phosphorescence is significantly larger for **Rh123-2Br** than for **Rh123**.

The distance to the NP for the largest ϕ'_{phos} is much shorte than 10–12 nm, where $\varphi_{fl}(S_1 \rightarrow S_0)$ reaches its maximum.[3,56] The energy transfer from the T_1 state to the NP is less efficient than from the S_1 state because $\vec{p}'' = \left\langle \psi(\tilde{T}_1)|\vec{p}''|\psi(\tilde{S}_0)\right\rangle$ in eqn (30) and (31) is two to three orders of magnitude larger than $\langle\psi(S_1)|\vec{p}|\psi(S_0)\rangle$.

When the molecule approaches a NP, the quantum yield from S_1 to T_1 decreases due to an efficient energy transfer from S_1 to the Ag NP that appears at a distance of 10–12 nm. The rate constant for this process is 10^{10}–10^{11} s^{-1}, which is much faster than the $k_{ISC}(S_1 \rightarrow T_1)$ process at a distance of 5–6 nm. The population of T_1 is significantly smaller at this distance, where the efficiency of the phosphorescence enhancement also decreases due to the smaller probability for populating the T_1 state as compared to the energy transfer from S_1 to the NP.

5. Conclusions

A theoretical model is proposed that enables estimation of the quantum yield of phosphorescence of a molecule near a plasmonic NP. The rate constants of radiative (k_r, k_{phos}) and

Table 4 Changes in the rate constants of fluorescence (k_r in s^{-1}) and phosphorescence (k_{phos} in s^{-1}) with and without the Ag NPs are estimated using the experimental parameters in eqn (33). The largest $k_{phos}(\tilde{T}_1 \rightarrow \tilde{S}_0)$ (in s^{-1}) and $\varphi_{phos}(\tilde{T}_1 \rightarrow \tilde{S}_0)$ values that were obtained in the calculations are also reported

Dye	k_r^{glass}	k_r^{SIF}	k_r^{SIF}/k_r^{glass}	k_{phos}^{glass}	k_{phos}^{SIF}	$k_{phos}^{SIF}/k_{phos}^{glass}$
Experimental						
Rh123	2.4×10^8	12.7×10^8	5.3	1.2	5.7	4.8
Rh123-2Br	1.9×10^8	10.6×10^8	5.0	1.04×10^2	8.84×10^2	8.5

	$k_{phos}(\tilde{T}_1 \rightarrow \tilde{S}_0)$	$k'_{phos}\left(\tilde{T}_1 \rightarrow \tilde{S}_0\right)$	$\frac{k'_{phos}\left(\tilde{T}_1 \rightarrow \tilde{S}_0\right)}{k_{phos}\left(\tilde{T}_1 \rightarrow \tilde{S}_0\right)}$	$\varphi_{phos}(\tilde{T}_1 \rightarrow \tilde{S}_0)$	$\phi'_{phos}\left(\tilde{T}_1 \rightarrow \tilde{S}_0\right)$	$\frac{\phi'_{phos}\left(\tilde{T}_1 \rightarrow \tilde{S}_0\right)}{\phi_{phos}\left(\tilde{T}_1 \rightarrow \tilde{S}_0\right)}$
Calculated						
Rh123	1.2	15.2	12.7	0.23	0.66	2.9
Rh123-2Br	1.5	39.1	26.1	0.002	0.064	32.0

nonradiative intramolecular transitions (k_{IC}, k_{ISC}, k_{RISC}) are calculated for estimating the quantum yields of fluorescence and phosphorescence. The developed model was tested on rhodamine and brominated rhodamine. Calculations of the lowest excitation energies yielded values in good agreement with experimental data for the $S_1 \rightarrow S_0$ and $T_1 \rightarrow S_0$ transitions. The calculated fluorescence quantum yields are also in good agreement with experimental values.

The energy difference between the S_1 and T_1 states (ΔE_{ST}) is 2661 and 1855 cm^{-1} for **Rh123** and **Rh123-2Br**, respectively leading to a $k_{ISC}(S_1 \rightarrow T_1)$ rate constant for **Rh123-2Br** that is two orders of magnitude larger than for **Rh123**. The Br atoms of **Rh123-2Br** increase the spin–orbit coupling matrix elements $\langle T_1|H_{SO}|S_0\rangle$ and $\langle S_1|H_{SO}|T_1\rangle$ by a factor of 3 and 2 as compared to those of **Rh123**. However, the $k_{ISC}(T_1 \rightarrow S_0)$ rate constant does not significantly affect to the total lifetime of the triplet state because the transition is very slow due to the large excitation energy of the triplet state.

The $k_{RISC}(T_1 \rightarrow S_1)$ rate constant of **Rh123-2Br** is two orders of magnitude larger than for **Rh123**. The larger rate constant of reverse ISC for **Rh123-2Br** leads to a significantly smaller quantum yield of phosphorescence than for **Rh123**. The reversed ISC process from T_1 to S_1 that enables thermally activated delayed fluorescence is also observed experimentally.

The luminescence processes of the studied molecules are faster in the presence of a plasmonic NP. The plasmonic effect increases the rate of the direct fluorescence by a factor of 5. The plasmonic effect on the delayed fluorescence (DF) and phosphorescence is larger for **Rh123-2Br** than for **Rh123** because the intensity borrowing of the spin-forbidden triplet–singlet transition ($T_1 \rightarrow S_0$) from the spin-allowed allowed $S_n \rightarrow S_0$ transitions is more significant for molecules with heavy atoms. The largest increase in the phosphorescence efficiency is obtained when the molecule is 4–5 nm from the NP surface, which also agrees with experimental observations.[47]

The results obtained in the present study support the design of plasmon-enhanced nanostructures that can be used in light-emitting media, in organic light emitting diodes (OLED), in photovoltaic devices and as catalysts for producing singlet oxygen.

Author contributions

All authors have discussed the results and contributed to the final manuscript. N. I.: conceptualization, methodology, resources, project administration, writing – review and editing; R. V.: methodology, conceptualization, calculations; modelling, data validation and visualization, software, writing – original draft; E. S.: investigation, data curation, data validation and visualization, writing – original draft; E. M.: investigation, formal analysis; R. N.: calculations; modelling, data validation and visualization; D. S.: conceptualization, data validation, writing – review and editing.

Conflicts of interest

There are no conflicts to declare.

Acknowledgements

This research is funded by the Science Committee of the Ministry of Science and Higher Education of the Republic of Kazakhstan (Grant No. AP14870117). This work has been supported by the Academy of Finland through projects 340582 (RRV) and 340583 (DS). We thank CSC – IT Center for Science, Finland for computer time.

References

1 L. Novotny and B. Hecht, *Principles of Nano-Optics*, Cambridge University Press, Cambridge, 2006.
2 R. K. Harrison and A. Ben-Yakar, *Opt. Express*, 2010, **18**, 22556–22571.
3 P. Anger, P. Bharadwaj and L. Novotny, *Phys. Rev. Lett.*, 2006, **96**, 113002.
4 E. Seliverstova, N. Ibrayev, G. Omarova, A. Ishchenko and M. Kucherenko, *J. Lumin.*, 2021, **235**, 118000.
5 C. D. Geddes and J. R. Lakowicz, *J. Fluoresc.*, 2002, **12**, 121–129.
6 V. Krivenkov, P. Samokhvalov, I. Nabiev and Y. P. Rakovich, *J. Phys. Chem. Lett.*, 2020, **11**, 8018–8025.
7 P. Kumbhakar, S. Biswas and P. Kumbhakar, *RSC Adv.*, 2019, **9**, 37705.
8 N. K. Ibrayev and A. K. Aimukhanov, *Opt. Laser Technol.*, 2019, **115**, 246–250.
9 E. V. Seliverstova and N. K. Ibrayev, *J. Phys.: Conf. Ser.*, 2016, **735**, 012018.
10 A. K. Aimukhanov and N. K. Ibrayev, *J. Lumin.*, 2018, **204**, 216–220.
11 P. C. Lee and D. Meisel, *J. Phys. Chem.*, 1982, **86**, 3391–3395.
12 G. A. Baker, *J. Am. Chem. Soc.*, 2005, **127**, 14118–14119.
13 Y. Wang and T. Ding, *Nanoscale*, 2019, **11**, 10589–19594.
14 F. Shaik, I. Peer, P. K. Jain and L. Amirav, *Nano Lett.*, 2018, **18**, 4370–4376.
15 R. Ranjan, E. N. Esimbekova, M. A. Kirillova and V. A. Kratasyuk, *Anal. Chim. Acta*, 2017, **971**, 1–13.
16 E. V. Seliverstova, N. K. Ibrayev and A. Z. Zhumabekov, *Opt. Spectrosc.*, 2020, **128**, 1449–1457.
17 R. Knoblauch, B. Bui, A. Raza and C. D. Geddes, *Phys. Chem. Chem. Phys.*, 2018, **20**, 15518–15527.
18 J. Niklas, A. Agostini, D. Carbonera, V. M. Di and W. Lubitz, *Photosynth. Res.*, 2022, **152**, 213–234.
19 P. S. Maharjan and H. K. Bhattarai, *J. Oncol.*, 2022, **2022**, 7211485.
20 A. A. Ishchenko and A. T. Syniugina, *Theor. Exp. Chem.*, 2023, **58**, 373–401.
21 J. Dolanský, P. Henke, Z. Malá, L. Žárská, P. Kubát and J. Mosinger, *Nanoscale*, 2018, **10**, 2639–2648.
22 T. Maisch, J. Baier, B. Franz, M. Maier, M. Landthaler, R. M. Szeimies and W. Bäumler, *Proc. Natl. Acad. Sci. U. S. A.*, 2007, **104**, 7223–7228.
23 B. Minaev, *Arch. Pulmonol. Respir. Care*, 2022, **8**, 028–033.
24 M. P. Rayaroth, U. K. Aravind, G. Boczkaj and C. T. Aravindakumar, *Chemosphere*, 2023, **345**, 140203.

25 A. Sagadevan, K. Ch Hwang and M.-D. Su, *Nat. Commun.*, 2017, **8**, 1812.
26 R. Schmidt, *Photochem. Photobiol.*, 2006, **82**, 1161–1177.
27 M. Bregnhøj, M. Prete, V. Turkovic, A. U. Petersen, M. B. Nielsen, M. Madsen and P. R. Ogilby, *Methods Appl. Fluoresc.*, 2020, **8**, 014001.
28 J. E. Guillet, J. Sherren, H. M. Gharapetian and W. K. MacInnis, *J. Photochem.*, 1984, **25**, 501–509.
29 F. Li, A. J. Gillett, Q. Gu, J. Ding, Z. Chen, T. J. H. Hele, W. K. Myers, R. H. Friend and E. W. Evans, *Nat. Commun.*, 2022, **13**, 2744.
30 L. E. de Sousa, L. dos Santos Born, P. H. de Oliveira Neto and P. de Silva, *J. Mater. Chem. C*, 2022, **10**, 4914–4922.
31 L. Naimovičius, P. Bharmoria and K. Moth-Poulsen, *Mater. Chem. Front.*, 2023, **7**, 2297–2315.
32 J. Jin, T. Yu, J. Chen, R. Hu, G. Yang, Y. Zeng and Y. Li, *Curr. Opin. Green Sustainable Chem.*, 2023, **43**, 100841.
33 C. Gao, A. Shukla, H. Gao, Z. Miao, Y. Zhang, P. Wang, G. Luo, Y. Zeng, W. W. H. Wong, T. A. Smith, S. C. Lo, W. Hu, E. B. Namdas and H. Dong, *Adv. Mater.*, 2023, **35**, 2208389.
34 E. B. Namdas, B. B. Y. Hsu, Z. Liu, S. C. Lo, P. L. Burn and I. D. W. Samuel, *Adv. Mater.*, 2009, **21**, 4957–4961.
35 H. Mishra, B. L. Mali, J. Karolin, A. I. Dragan and C. D. Geddes, *Phys. Chem. Chem. Phys.*, 2013, **15**, 19538–19544.
36 Y. Zhang, K. Aslan, M. J. R. Previte, S. N. Malyn and C. D. Geddes, *J. Chem. Phys. B*, 2006, **110**, 25108–25114.
37 M. Meng, F.-L. Zhang, J. Yi, L.-H. Lin, C.-L. Zhang, N. Bodappa, C.-Y. Li, S.-J. Zhang, R. F. Aroca, Z.-Q. Tian and J.-F. Li, *Anal. Chem.*, 2018, **90**, 10837–10842.
38 S. Bidault, A. Devilez, V. Maillard, L. Lermusiaux, J.-M. Guigner, N. Bonod and J. Wenger, *ACS Nano*, 2016, **10**, 4806–4815.
39 H. Wang, J. Jung, K. Chung, J. W. Lim, Y. You, J. Kim and D. H. Kim, *J. Appl. Phys.*, 2017, **122**, 153103.
40 R. Lakshmanan, N. C. Shivaprakash and S. Sindhu, *J. Lumin.*, 2018, **196**, 136–145.
41 X. Cao, B. Hu, R. Ding and P. Zhang, *Phys. Chem. Chem. Phys.*, 2015, **17**, 14479–14483.
42 N. L. Pacioni, M. González-Béjar, E. Alarcón, K. L. McGilvray and J. C. Scaiano, *J. Am. Chem. Soc.*, 2010, **132**, 6298–6299.
43 B. V. Enustun and J. Turkevich, *J. Am. Chem. Soc.*, 1963, **85**, 3317–3328.
44 N. Takeshima, K. Sugawa, H. Tahara, S. Jin, H. Wakui, M. Fukushima, K. Tokuda, S. Igari, K. Kanakubo, Y. Hayakawa, R. Katoh, K. Takase and J. Otsuki, *ACS Nano*, 2019, **13**, 13244–13256.
45 J. Ostrowski, A. Mikhailovsky, D. Bussian, M. Summers, S. Buratto and G. Bazan, *Adv. Funct. Mater.*, 2006, **16**, 1221–1227.
46 C. Seo, J. Lee, M. S. Kim, Y. Lee, J. Jung, H.-W. Shin, T. K. Ahn, G. Sun, J. Kim and J. Kim, *Chem. Phys. Lett.*, 2017, **676**, 134–139.
47 D. Temirbayeva, N. Ibrayev and M. Kucherenko, *J. Lumin.*, 2022, **243**, 118642.
48 T. M. Chmereva, M. G. Kucherenko, F. Yu Mushin and A. P. Rusinov, *J. Appl. Spectrosc.*, 2024, **91**, 1–9.
49 S. P. McGlynn, T. Azumi and M. Kinoshita, *Molecular Spectroscopy of the Triplet State*, Prentice-Hall, Inc., Englewood Cliffs, New Jersey, 1969.
50 R. Valiev, V. N. Cherepanov, G. V. Baryshnikov and D. Sundholm, *Phys. Chem. Chem. Phys.*, 2018, **20**, 6121–6133.
51 R. R. Valiev, R. T. Nasibullin, V. N. Cherepanov, A. Kurtsevich, D. Sundholm and T. Kurtén, *Phys. Chem. Chem. Phys.*, 2021, **23**, 6344–6348.
52 R. R. Valiev, V. N. Cherepanov, R. T. Nasibullin, D. Sundholm and T. Kurten, *Phys. Chem. Chem. Phys.*, 2019, **21**, 18495–18500.
53 R. R. Valiev, B. S. Merzlikin, R. T. Nasibullin, A. Kurtzevitch, V. N. Cherepanov, R. R. Ramazanov, D. Sundholm and T. Kurten, *Phys. Chem. Chem. Phys.*, 2023, **25**, 6406–6415.
54 S. Perun, J. Tatchen and C. M. Marian, *ChemPhysChem*, 2008, **9**, 282–292.
55 J. Tatchen and C. M. Marian, *Phys. Chem. Chem. Phys.*, 2006, **8**, 2133–2144.
56 N. Kh Ibrayev, E. V. Seliverstova, R. R. Valiev, A. E. Kanapina, A. A. Ishchenko, A. V. Kulinich, T. Kurten and D. Sundholm, *Phys. Chem. Chem. Phys.*, 2023, **25**, 22851–22861.
57 W. Feng, L. Xu, X.-Q. Li, W. Fang and Y. Yan, *AIP Adv.*, 2014, **4**, 077131.
58 J. Cao and Z.-Z. Xie, *Phys. Chem. Chem. Phys.*, 2016, **18**, 6931–6945.
59 J. C. Vincenta and F. Furche, *Phys. Chem. Chem. Phys.*, 2013, **15**, 18336–18348.
60 G. Baryshnikov, B. Minaev and H. Ågren, *Chem. Rev.*, 2017, **117**, 6500–6537.
61 H. Ågren, B. F. Minaev and S. Knuts, *J. Phys. Chem.*, 1994, **98**, 3943–3949.
62 R. R. Valiev, I. Benkyi, Y. V. Konyshev, H. Fliegl and D. Sundholm, *J. Phys. Chem. A*, 2018, **122**, 4756–4767.
63 R. R. Valiev, B. S. Merzlikin, R. T. Nasibullin, V. N. Cherepanov, D. Sundholm and T. Kurtén, *Phys. Chem. Chem. Phys.*, 2024, **26**, 4151–4158.
64 R. R. Valiev, R. T. Nasibullin, B. S. Merzlikin, K. Khoroshkin, V. N. Cherepanov and D. Sundholm, *Phys. Chem. Chem. Phys.*, 2024, **26**, 2945–2950.
65 B. Merzlikin, V. Cherepanov, K. Khoroshkin and R. Valiev, *Chem. Phys. Lett.*, 2023, **836**, 141032.
66 D. N. Butorina, A. A. Krasnovsky, L. P. Savvina and N. A. Kuznetsova, *Russ. J. Phys. Chem.*, 2005, **79**, 791–794.
67 R. S. Harapanhalli, A. M. Roy, S. J. Adelstein and A. I. Kassis, *J. Med. Chem.*, 1998, **41**, 2111–2117.
68 K. Aslan, Z. Leonenko, J. R. Lakowicz and C. D. Geddes, *J. Fluoresc.*, 2005, **15**, 643–654.
69 C. Würth, M. G. González, R. Niessner, U. Panne, C. Haisch and U. R. Genger, *Talanta*, 2012, **90**, 30–37.
70 R. R. Valiev, V. N. Cherepanov, V. Y. Artyukhov and D. Sundholm, *Phys. Chem. Chem. Phys.*, 2012, **14**, 11508–115017.
71 R. Valiev, V. N. Cherepanov, G. V. Baryshnikov and D. Sundholm, *Phys. Chem. Chem. Phys.*, 2018, **20**, 6121–6133.
72 J. Strickler and R. A. Berg, *Chem. Phys. Lett.*, 1964, **37**, 814–822.
73 E. S. Medvedev and V. I. Osherov, *Radiationless Transitions in Polyatomic Molecules*, Springer-Verlag, Berlin, 1995.

74 C. M. Marian, *Wiley Interdiscip. Rev.: Comput. Mol. Sci.*, 2012, **2**, 187–203.
75 R. M. Gadirov, R. R. Valiev, L. G. Samsonova, K. M. Degtyarenko, N. V. Izmailova, A. V. Odod, S. S. Krasnikova, I. K. Yakushchenko and T. N. Kopylova, *Chem. Phys. Lett.*, 2019, **717**, 53–58.
76 V. G. Plotnikov, *Int. J. Quantum Chem.*, 1979, **16**, 527–541.
77 V. L. Ermolaev, *Opt. Spectrosc.*, 2016, **121**, 567–584.
78 R. R. Valiev, R. T. Nasibullin, V. N. Cherepanov, G. V. Baryshnikov, D. Sundholm, H. Ågren, B. F. Minaev and T. Kurtén, *Phys. Chem. Chem. Phys.*, 2020, **22**, 22314–22323.
79 A. O. Govorov, J. Lee and N. A. Kotov, *Phys. Rev. B: Condens. Matter Mater. Phys.*, 2007, **76**, 125308.
80 M. G. Kucherenko and V. M. Nalbandyan, *Phys. Proc.*, 2015, **73**, 136–142.
81 P. Drude, *Ann. Phys.*, 1900, **306**, 566–613.
82 P. Drude, *Ann. Phys.*, 1900, **308**, 369–402.
83 A. Sommerfeld, *Z. Med. Phys.*, 1928, **47**, 1–32.
84 O. F. Mossotti, *Memorie di matematica e di fisica della Societá italiana delle scienze*, Presso La Società Tipografica, Verona, 1850, vol. 2, pp. 49–74.
85 R. Clausius, *Die mechanische Behandlung der Electricität*, Vieweg + Teubner Verlag, Wiesbaden, 1879.
86 M. J. Frisch, G. W. Trucks, H. B. Schlegel, G. E. Scuseria, M. A. Robb, J. R. Cheeseman, G. Scalmani, V. Barone, G. A. Petersson, H. Nakatsuji, X. Li, M. Caricato, A. V. Marenich, J. Bloino, B. G. Janesko, R. Gomperts, B. Mennucci, H. P. Hratchian, J. V. Ortiz, A. F. Izmaylov, J. L. Sonnenberg, D. Williams-Young, F. Ding, F. Lipparini, F. Egidi, J. Goings, B. Peng, A. Petrone, T. Henderson, D. Ranasinghe, V. G. Zakrzewski, J. Gao, N. Rega, G. Zheng, W. Liang, M. Hada, M. Ehara, K. Toyota, R. Fukuda, J. Hasegawa, M. Ishida, T. Nakajima, Y. Honda, O. Kitao, H. Nakai, T. Vreven, K. Throssell, J. A. Montgomery, Jr., J. E. Peralta, F. Ogliaro, M. J. Bearpark, J. J. Heyd, E. N. Brothers, K. N. Kudin, V. N. Staroverov, T. A. Keith, R. Kobayashi, J. Normand, K. Raghavachari, A. P. Rendell, J. C. Burant, S. S. Iyengar, J. Tomasi, M. Cossi, J. M. Millam, M. Klene, C. Adamo, R. Cammi, J. W. Ochterski, R. L. Martin, K. Morokuma, O. Farkas, J. B. Foresman and D. J. Fox, *Gaussian 16, Revision C.01*, Gaussian, Inc., Wallingford CT, 2016.
87 A. A. Granovsky, *J. Chem. Phys.*, 2011, **134**, 214113.
88 A. A. Granovsky, *Firefly version 8.0.0*, **https://classic.chem.msu.su/gran/firefly/index.html**.
89 C. A. Parker, *Photoluminescence of Solutions*, Elsevier Publishing Co., Amsterdam, 1968.
90 C. J. Chiang, A. Kimyonok, M. K. Etherington, G. C. Griffiths, V. Jankus, F. Turksoy and A. P. Monkman, *Adv. Funct. Mater.*, 2013, **23**, 739–746.
91 T. J. Penfold, F. B. Dias and A. P. Monkman, *Chem. Commun.*, 2018, **54**, 3926–3935.
92 R. R. Valiev, B. F. Minaev, R. M. Gadirov, E. N. Nikonova, T. A. Solodova, S. Y. Nikonov, M. B. Bushuev and T. N. Kopylova, *Russ. Phys. J.*, 2016, **58**, 1205–1211.